Am J Physiol Heart Circ Physiol 326: H166–H179, 2024.
First published November 10, 2023; doi:10.1152/ajpheart.00582.2023

american physiological society

AMERICAN JOURNAL OF PHYSIOLOGY
HEART AND CIRCULATORY PHYSIOLOGY

RESEARCH ARTICLE

Molecular and Cellular Physiology of Heart Failure and Cardiomyopathy

Ischemia-reperfusion myocardial infarction induces remodeling of left cardiac-projecting stellate ganglia neurons

Madeleine S. Barrett, Temerity C. Bauer, Ming-Hua Li, Deborah M. Hegarty, Clarissa M. D. Mota, Chimezie J. Amaefuna, Susan L. Ingram, Beth A. Habecker, and Sue A. Aicher

Department of Chemical Physiology and Biochemistry, Oregon Health and Science University, Portland, Oregon, United States

Abstract

Neurons in the stellate ganglion (SG) provide sympathetic innervation to the heart, brown adipose tissue (BAT), and other organs. Sympathetic innervation to the heart becomes hyperactive following myocardial infarction (MI). The impact of MI on the morphology of cardiac sympathetic neurons is not known, but we hypothesized that MI would stimulate increased cell and dendritic tree size in cardiac neurons. In this study, we examined the effects of ischemia-reperfusion MI on sympathetic neurons using dual retrograde tracing methods to allow detailed characterization of cardiac- and BAT-projecting neurons. Different fluorescently conjugated cholera toxin subunit B (CTb) tracers were injected into the pericardium and the interscapular BAT pads, respectively. Experimental animals received a 45-min occlusion of the left anterior descending coronary artery and controls received sham surgery. One week later, hearts were collected for assessment of MI infarct and SGs were collected for morphological or electrophysiological analysis. Cardiac-projecting SG neurons from MI mice had smaller cell bodies and shorter dendritic trees compared with sham animals, specifically on the left side ipsilateral to the MI. BAT-projecting neurons were not altered by MI, demonstrating the subpopulation specificity of the response. The normal size and distribution differences between BAT- and cardiac-projecting stellate ganglion neurons were not altered by MI. Patch-clamp recordings from cardiac-projecting left SG neurons revealed increased spontaneous excitatory postsynaptic currents despite the decrease in cell and dendritic tree size. Thus, increased dendritic tree size does not contribute to the enhanced sympathetic neural activity seen after MI.

NEW & NOTEWORTHY Myocardial infarction (MI) causes structural and functional changes specifically in stellate ganglion neurons that project to the heart, but not in cells that project to brown adipose fat tissue.

morphology; neural plasticity; sympathetic; tract tracing

INTRODUCTION

Myocardial infarction (MI) remains a leading cause of death worldwide, and patients who survive an MI have an elevated risk of ventricular arrythmias and sudden cardiac death (1–3). Sympathetic dysfunction is involved in triggering these ventricular arrythmias, and blocking sympathetic transmission decreases the incidence of severe arrhythmias and prolongs life after MI (4–8). The mechanisms by which sympathetic transmission contributes to arrhythmias have not been fully delineated. Several studies suggest sympathetic neuron structural remodeling following cardiac injury, including increased cell and dendritic tree size accompanied by synapse formation (9–13). Sympathetic innervation of the heart derives primarily from the stellate ganglion (SG) (14–16), though these ganglia house many populations of neurons innervating various other organs, including interscapular brown adipose tissue (BAT) (17). Neural plasticity following MI has been examined previously at different times after cardiac injury in different species (9, 12, 13, 18, 19), but prior studies have not selectively examined cardiac-projecting neurons or compared changes between different populations of SG neurons to delineate the specificity of morphological changes.

In the present study, we use dual tract tracing (20) to retrogradely label two distinct neuron populations within the same ganglia and assess the specificity of ischemia-reperfusion MI-induced morphological changes. The aims of this study were threefold: *1*) to assess the impact of ischemia-reperfusion MI on the morphology of cardiac- and BAT-projecting neurons in the SG after 1 wk, *2*) determine the specificity of neural plasticity in both subpopulations, based on their innervated targets, and *3*) assess functional changes in the subpopulation of cardiac-projecting

Correspondence: S. A. Aicher (aichers@ohsu.edu).
Submitted 19 September 2023 / Revised 23 October 2023 / Accepted 8 November 2023

neurons. We hypothesized that MI would increase cell size and dendritic field size in cardiac- but not BAT-projecting SG neurons.

MATERIALS AND METHODS

Experimental Animals

Male and female C57Bl/6J mice acquired from The Jackson Laboratory were used in these studies (22–33 g, 19–22 wk old). A total of 29 mice (15 males, 14 females) were used. Ten mice (5 males, 5 females) were allocated for morphological studies, 11 mice (6 males, 5 females) were used for electrophysiological studies, and 8 mice (4 males, 4 females) were used for mRNA quantification. Mice were housed in a 12-h light/dark cycle with access to food and water ad libitum. All experimental procedures were approved by the Oregon Health & Science University Institutional Animal Care and Use Committee and comply with the *Guide for the Care and Use of Laboratory Animals* published by the National Academies Press (8th ed.). Reporting of animal experiments conforms to the principles and regulations for animal experimental reporting and ethics in the Animal Research: Reporting of In Vivo Experiments (ARRIVE) guidelines (21).

General Surgical Procedures

Mice were anesthetized by inhalation of isoflurane (4% to induce, 2% to maintain in 100% oxygen) and core body temperature was monitored by a rectal probe and maintained at 37°C with a heating pad during all surgical procedures. A two-lead electrocardiogram (ECG) monitored cardiac rhythm throughout surgical procedures using a PowerLab and LabChart software (AD Instruments). Mice were intubated and mechanically ventilated during cardiac tracer and MI procedures described in *Cardiac Tracer Injections* and *Myocardial Infarction* and *Sham Procedures*. Following all procedures and wound closure, analgesics (0.1 mg/kg buprenorphine and 5 mg/kg meloxicam) and 0.5-mL lactated Ringer solution were administered subcutaneously. Mice were monitored in a heated, oxygen-supplied chamber (100% O_2, 2 L/min) during recovery from procedures, and were then housed individually and monitored daily following surgery.

Cardiac Tracer Injections

A left lateral thoracotomy was performed between the left third and fourth rib to expose the heart. The tract tracer was manually injected into the pericardial sac of each animal as previously described (20). The pericardium remained intact for 10 min following pericardial CTb injection to allow for neuronal tracer uptake before proceeding to myocardial infarction and sham procedures (see below). Each animal received a 10-μL volume injection of tracer into the pericardial space using a 10-μL syringe (Hamilton). The tracer, cholera toxin subunit B (CTb) conjugated to Alexa Fluor (AF) 555 (Invitrogen Thermo Fisher Scientific, C22843), was diluted in 0.01 M PBS at a concentration of 1 mg/mL.

Myocardial Infarction and Sham Procedures

Myocardial infarction (MI) was generated by ischemia-reperfusion as previously described (22, 23). Ten minutes following the pericardial CTb injection, the pericardial sac was torn to visualize the left anterior descending coronary artery (LAD), which was ligated for 45 min with 8-0 suture (Covidien). Occlusion was confirmed by sustained S-T segment elevation on ECG (22, 24) and the presence of cyanosis in the myocardium distal to the LAD occlusion. Release of the ligation prompted reperfusion that was verified by the return of color to the ventricle and reperfusion arrhythmia visible on the ECG (22, 23, 25). Sham mice underwent the same procedure described except the LAD was not occluded. The thoracic cavity was closed, and mice were weaned off the ventilator.

For electrophysiology studies, a subset of mice underwent ischemia-reperfusion or sham procedures without prior administration of CTb (sham, 1 M, 2 F; MI 1 F). For isolation of cardiac mRNA, mice (2 M, 2 F) underwent ischemia-reperfusion without administration of CTb.

BAT Tracer Injections

After the MI or sham procedure, once the mouse was breathing without ventilator support, mice for the stellate morphology study were anesthetized via nose cone by inhalation of isoflurane (2% in 100% oxygen). A dorsal midline incision between the scapulae exposed both interscapular BAT deposits that were each injected with a total of 4 μL of 1 mg/mL CTb conjugated to AF 488 (Invitrogen Thermo Fisher Scientific, C22841) diluted in 0.01 M PBS. BAT deposits were manually injected twice per pad in different regions to ensure diffusion of the tracer through the adipose tissue, as previously described (20). BAT tracer injections were only performed on mice in the morphology study group.

Tissue Collection for Stellate Morphology Analysis and Infarct Size

Seven days following surgical procedures, mice were deeply anesthetized with isoflurane and euthanized by decapitation. Hearts were harvested and rinsed twice for 10 min in 0.01 M phosphate-buffered saline (PBS). The atria were removed, and the ventricles were fixed in 4% paraformaldehyde (PFA) in 0.01 M PBS for 1–1.5 h, rinsed 5 × 2 min in 0.01 M PBS, and incubated in 30% sucrose at 4°C until cryosectioning. The ventricles were sectioned at 12 μm on a cryostat, mounted on slides, and kept at −80°C until immunohistochemical processing.

Left and right SG, located lateral to the longus colli muscles and across the second rib, were removed and immediately fixed in 4% PFA in 0.1 M phosphate buffer (PB) for 30 min, rinsed in 0.1 M PB, and stored in cryoprotectant (30% sucrose/30% ethylene glycol in PB) at −20°C until processing (20) for immunohistochemistry.

Immunohistochemistry on Hearts and Infarct Size Analysis

Thawed slides of ventricle tissue sections were rinsed with 0.1 M PB for 10 min, incubated in 10 mg/mL $NaBH_4$ for 2 × 10 min, rinsed with 0.1 M PB followed by 0.1 M Tris-buffered saline pH 7.6 (TS), and placed in 0.3% Triton X-100 and 1% BSA in 0.1 M TS for 1 h. Tissues were incubated in a primary antibody solution of sheep anti-fibrinogen (1:300; Bio-Rad, RRID: AB_620402) in 0.1% BSA and 0.03% Triton X-100 in 0.1 M TS overnight at room temperature. Sections were then

rinsed with TS for 5 min and incubated for 90 min at room temperature in donkey anti-sheep AF 488 secondary antibody (1:500, Jackson Immuno Research) in 0.1% BSA in 0.1 M TS. Slides were coverslipped with ProLong Gold Antifade mountant (Thermo Fisher Scientific).

Images of cardiac tissue were acquired using a Keyence BZ-X 800 microscope at ×2 magnification. Five slides were chosen throughout the visible infarct and the region of fibrinogen labeling was delimited using the ImageJ freehand selection tool and quantified in ImageJ. The cardiac infarct size was calculated as the percentage of the left ventricle (including the intraventricular septum) stained for fibrinogen [(fibrinogen area/LV total area) × 100] by an investigator without knowledge of treatment groups. Criteria for inclusion in the infarct group was an infarct size of at least 15% of the combined left ventricle and septum.

Immunohistochemistry on Stellate Ganglia

Immunohistochemistry was performed on free-floating whole mount stellate ganglia (SG) as previously described (20). Paraformaldehyde-fixed SGs were rinsed for 4 × 5 min in 0.1 M PB and 3 × 5 min in 0.1 M TS, then placed in 0.5% bovine serum albumin (BSA, Sigma-Aldrich) in TS for 30 min. SGs were incubated for 48 h at 4°C in primary antibody solution of goat anti-vesicular acetylcholine transporter (VAChT, 1:1,000, EMD Millipore, RRID: AB-2630394), in 0.25% Triton X-100 (Sigma-Aldrich), and 0.1% BSA in 0.1 M TS. Then, SGs were rinsed with TS and incubated for 2 h at room temperature in donkey anti-goat AF 647 secondary antibody (1:800, Jackson Immuno Research) in 0.1% BSA in TS. SGs were rinsed, mounted on slides, and coverslipped using ProLong Gold Antifade mountant (TFS).

Confocal Scanning and Confocal Scan Analysis

Whole SG analysis of cell number, dispersion, and neuronal contacts.

To examine the number and distribution of retrogradely labeled SG neurons, confocal images were taken of the whole SG, using a Zeiss LSM 900 confocal microscope with a Plan-Apochromat ×20/0.8 M27 objective in the Advanced Light Microscopy Core (ALMC) at Oregon Health and Science University. Six 1,024 × 1,024-pixel frames of 25-μm *Z*-stacks taken at 1.5-μm intervals detecting AF 488 and AF 555 were stitched together postscan. Whole SG scans were assessed by two independent observers with no knowledge of treatment group. Neurons labeled with CTb AF 488 or CTb 555 were counted using Imaris 9.9.1 software (Bitplane, Oxford Instruments, UK). Images were preprocessed using a set threshold cutoff filter to reduce background on all channels. Cell bodies with an estimated 20-μm diameter were identified and marked via the automated spots wizard, then verified manually.

To characterize the distribution of cells in the SG, nearest neighbor distances (μm) were measured from the center of each identified cell body to the center of the nearest cell body of the same tracer group (cardiac or BAT) using Imaris 9.9.1, as previously described (20). We also assessed direct contacts between neurons within each subpopulation by identifying the number of spots that were <20 μm apart from another neuron using an Imaris filter, followed by manual confirmation by two treatment-blinded investigators that the cells were in direct contact. The number of neurons in contact with one or more other neurons (%coupled neurons) were counted and normalized to the total number of labeled neurons in each tracer subgroup.

High-resolution SG analysis for soma, dendrites, and VAChT puncta.

To study the structural components of SG neurons, high magnification 1,024 × 1,024-pixel confocal scans of CTb tracer-filled neurons (AF 488 or AF 555) were acquired capturing the soma, dendrites, and VAChT puncta using the Zeiss LSM 900 confocal microscope with a Plan-Apochromat ×40/1.4 oil objective at 0.24-μm *Z*-intervals at ×0.7 zoom. Neurons were selected for high-resolution imaging from six separate regions of the SG for three-dimensional (3-D) rendering (Imaris 9.9.1) and analysis (20).

Soma and VAChT reconstruction methods and criteria.

Soma and VAChT 3-D reconstructions were performed as previously described using the surface and spot segmentation tools in Imaris, respectively (20). Cell bodies containing AF-488 or AF-555 tracer entirely within the *XY* and *Z*-ranges of high-magnification ×40 confocal scans were isolated within a region of interest (ROI) boundary. A consistent smoothing level was applied, and each surface was manually constructed and reviewed by two investigators for accuracy. Imaris then calculated the volume (in mm^3) of each reconstructed soma.

VAChT puncta, fluorescently labeled with AF 647, within 0.5 mm of a reconstructed CTb AF 555 soma surface (cardiac-projecting SG neurons) were assessed using the spots tool in Imaris in ×40 confocal scans. To qualify for inclusion, VAChT puncta were required to have an *XY* diameter equal to or greater than 0.4 μm and a *Z* diameter equal to or greater than 0.3 μm. VAChT puncta within 0.5 μm of the soma surface were identified and counted per AF 555 neuron using an Imaris filter, which measured the distance from the soma surface to the center of each reconstructed VAChT puncta. Final puncta counts were verified visually.

Assessment of soma cross-sectional area.

To further assess soma size between treatment groups, the cross-sectional area (mm^2) was measured from the same high-magnification ×40 confocal scans of left SG cardiac-projecting neurons (CTb AF 555 tracer) as described for 3-D reconstruction in Imaris (above). To perform the cross-sectional analysis, confocal images were analyzed using Zeiss ZEN software from a representative slice of each neuron's *z*-stack containing the nucleus through the center of the cell. A free-form boundary was drawn around the selected section and the cross-sectional area (mm^2) was recorded for each cell.

Dendrite reconstruction methods and criteria.

Neurons with discernable dendritic branches (AF 488 and AF 555 CTb tracer) were semi-automatically traced based on fluorescence intensity using the Filaments tool in Imaris as previously described (20). For each reconstructed dendritic tree, the number of primary dendrites, dendritic branches, and total length of the dendritic tree were quantified as was

visible within the boundaries of each scan. Axons were identified as the least branched and longest process and were excluded from analysis when present. Neurons close to the edge of the scan, touching another cell, or with dendrites that could not be deciphered between two cells or from background fluorescence were excluded from dendritic analysis.

RNA Isolation and qPCR

Left ventricles were harvested from unoperated control hearts or 24 h after ischemia-reperfusion and stored immediately in RNAlater. RNA was isolated from the left ventricles using the Qiagen RNAeasy mini kit. Total RNA was quantified by OD260, and 200 ng of total RNA was treated with DNase and reverse-transcribed using random primers. Real-time PCR was performed with the ABI TaqMan Fast Universal PCR Master mix in the ABI 7500, using ABI prevalidated TaqMan gene expression assays for mouse bone morphogenetic proteins [BMP2 (Mm01340178_m1), BMP4 (Mm00432087_m1), BMP5 (Mm00432091_m1), BMP6 (Mm01332882_m1), BMP7 (Mm00432102_m1), and BMP10 (Mm01183889_m1)], with β actin as an internal control (Mm02619580_g1). For the PCR amplification, 2 μL of RT reactions were used in a total volume of 20 μL, and each sample was assayed in duplicate. BMP mRNAs were normalized to actin mRNA in the same sample. Ischemia-reperfusion did not regulate the expression of actin mRNA (23).

Electrophysiological Recordings from SG Neurons

Left stellate ganglion preparation.

Mice were deeply anaesthetized with isoflurane and decapitated 1 wk following MI or sham surgery. The left SG was quickly dissected out and incubated for 90 min at room temperature with continually oxygenated (95% O_2-5% CO_2) artificial cerebrospinal fluid (aCSF) containing collagenase (12.5 mg/mL collagenase from *Clostridium histolyticum* type II, Millipore-Sigma, St. Louis, MO). The aCSF contained (in mM) 126 NaCl, 2.5 KCl, 2.4 $CaCl_2$, 1.2 $MgCl_2$, 1.2 NaH_2PO_4, 21.4 $NaHCO_3$, and 11.1 D-glucose at pH 7.4, and the osmolarity was adjusted to 300–310 mosmol/L. Following digestion, the remaining connective and fatty tissues were removed carefully under a dissection microscope with fine forceps. The isolated ganglion was then placed in a recording chamber continuously perfused (2.0–3.0 mL/min) with warm (34°C) oxygenated aCSF for 30 min. Bath temperature was maintained and measured by a TC^2 bip temperature controller (Cell MicroControls, Norfolk, VA).

Whole cell recordings.

Electrophysiological recordings of stellate neurons were performed as previously described (26) with modifications. In the majority of ganglia, cardiac neurons were identified by the presence of the retrograde label CTb using fluorescence microscopy. In additional ganglia, presumed cardiac-projecting neurons were identified within the cardiac pole (20) under bright-field illumination (differential interference contrast; DIC). Spontaneous excitatory postsynaptic currents (sEPSCs) were recorded using whole cell voltage clamp (Multiclamp 700B; Molecular Devices, Union City, CA). Recordings were made with electrodes pulled to 2–3 MΩ resistance and filled with internal solution consisting of the following (in mM; pH 7.4): 138 potassium gluconate, 10 HEPES, 10 KCl, 1 $MgCl_2$, 1 EGTA, 0.3 $CaCl_2$, 4 MgATP, and 3 NaGTP. Series resistance (<20 MΩ) was continuously monitored during experiments. Recordings in which series resistance or capacitance changed by >15% during the experiment were excluded from data analysis. Events were low-pass filtered at 2 kHz and digitized at 20 kHz using a Digidata 1550B for online and later offline analysis. Individual events were detected offline using Clampfit 11.0 software (Molecular Devices) and visually confirmed. sEPSCs with amplitude <10 pA were excluded from the analysis.

Statistical Analysis

Statistical testing for morphology measurements was performed using SigmaPlot v14.5 (SyStat/Inpixon software) with significance set to $P = 0.05$. Statistical testing for electrophysiology and mRNA data was performed using GraphPad Prism v10. Parametric statistical tests such as *t* tests (with or without Welch's correction) and two- and three-way ANOVAs were used when appropriate to compare between treatment groups, left and right stellate ganglia, and cell types (cardiac or BAT). In some cases, data were rank-transformed to meet normality and equal variance requirements for parametric tests. Nonparametric statistical tests such as Mann–Whitney rank sum tests and Kruskal–Wallis one-way ANOVA on ranks were used when normality and equal variance requirements were not met. Post hoc comparisons were used as appropriate. See RESULTS for specific statistical tests used for each comparison.

RESULTS

Ischemia-Reperfusion Produces Cardiac Infarct

To ensure that stellate morphology comparisons used ganglia from animals with a similar degree of cardiac damage, we assessed infarct size in multiple sections from each heart. Postmortem analysis of fibrinogen immunohistochemistry was used to identify the infarcted area in heart sections (Fig. 1*A*). The cardiac infarct size was significantly larger in MI mice than in sham controls (Fig. 1*B*; Mann–Whitney rank-sum test, $P = 0.02$). Hearts that did not have an infarct covering at least 15% of the left ventricle after ischemia-reperfusion surgery were excluded from the study.

MI Does Not Alter Number or Distribution of Cardiac- or BAT-Projecting SG Neurons

To assess the impact of each surgery (MI or sham) on the number of tracer-labeled cardiac- and BAT-projecting neurons in the SG, we counted the number of CTb AF 555- and AF 488-labeled cells from each injection target (heart and BAT). We found that MI did not change the number of retrogradely labeled cardiac- or BAT-projecting neurons in the SG as compared with sham [Table 1; two-way ANOVAs on treatment (MI/sham) and side (left/right) for cardiac- and BAT-projecting SG neurons].

The qualitative distribution of the labeled neurons was similar to what we have found previously (20). Specifically, whole SG confocal scans showed cardiac-projecting neurons aggregating medially around the inferior cardiac nerve (Fig. 2), whereas BAT-projecting neurons appeared evenly distributed

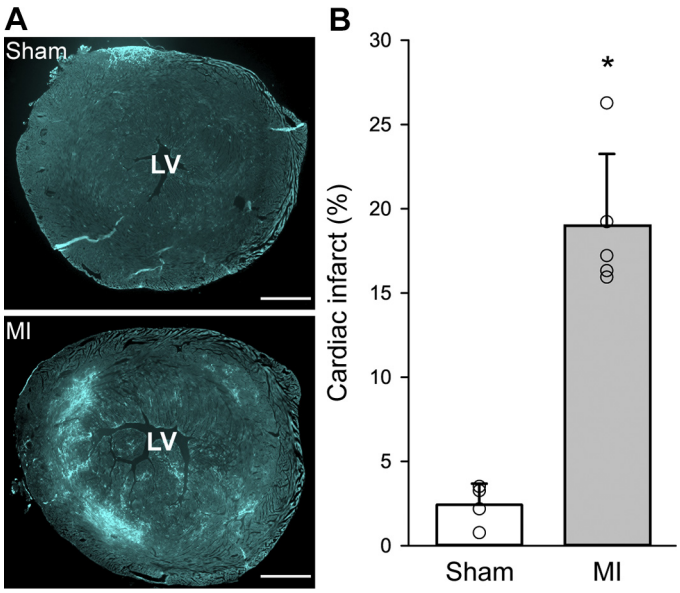

Figure 1. Cardiac infarct size assessed by fibrinogen labeling of heart sections was greater after myocardial infarction (MI) than sham surgery. *A*: representative images of fibrinogen labeling in sections through the left ventricle (LV) of the heart from a sham (*top*) and MI (*bottom*) mouse. *B*: infarct size quantified as percent area of left ventricle. Bars represent means ± SD and open circles represent individual values for each heart ($n = 4$ sham, 5 MI mice). Scale bars = 1 mm. MI vs. sham, Mann–Whitney rank sum test: $^*P = 0.02$.

throughout the ganglia (Fig. 2). One animal in the BAT-projecting group had a low amount of retrograde labeling (Table 1); however, treatment did not alter the overall number of retrogradely labeled neurons or their qualitative distribution within the SG (Table 1 and Fig. 2).

MI Reduces the Size of Cardiac-Projecting Left SG Neurons

To test the hypothesis that MI would alter the morphology of cardiac- and/or BAT-projecting neurons, cells were 3-D-rendered using Imaris software to assess soma volume (μm^3) and other structural features (Fig. 3); the neurons reconstructed for each morphological assessment are found in Table 1 (Soma Reconstructed), which were selected based on the criteria described in MATERIALS AND METHODS. We found that cardiac-projecting cell bodies in the left SG are smaller in MI-treated mice compared with left SG neurons in sham mice [Fig. 4*A*; Kruskal–Wallis one-way ANOVA on ranks ($P = 0.011$), Dunn's post hoc pairwise comparisons; $P = 0.03$] and right SG neurons in MI mice (Dunn's post hoc pairwise comparisons; $P = 0.02$) 1 wk after treatment. There was no size difference between MI- and sham-treated cardiac-projecting neurons in the right SG (Fig. 4*A*). There were no differences in the soma size of BAT-projecting neurons in either left or right SG between treatment groups (Fig. 4*A*; Kruskal-Wallis one-way ANOVA on ranks).

To further characterize the impact of MI on soma size, we measured the cross-sectional area (μm^2) of cardiac-projecting neurons in the left SG (see Table 1 for number of neurons analyzed). The MI treatment group had significantly smaller left SG cardiac somas compared with sham (Fig. 4*B*; unpaired Welch's *t* test; $P = 0.02$). This alternative method used a different image analysis software, Zen, and confirmed that MI reduces cardiac-projecting SG neuron soma size in the left SG.

To characterize the dispersion pattern of cardiac-projecting neurons in the SG, we measured the distance from the center of each neuron to the center of the nearest neighboring cell within each neuronal group (Fig. 5; $n = 616$ sham left, 587 sham right, 615 MI left, and 639 MI right neurons). There was an overall significant difference in mean distance measurements among the groups (Kruskal–Wallis one-way ANOVA on ranks, $P < 0.001$). Cardiac-projecting left SG neurons in the MI treatment group were more distant from their nearest neighboring cells when compared with neurons in the right MI SG, as well as the left and right sham SGs (Dunn's post hoc pairwise comparisons; $P < 0.001$ for all pairs).

Cardiac-Projecting SG Neurons Are "Coupled" More Often than BAT-Projecting SG Neurons

We assessed the number of neurons in direct contact ("coupled") within each SG neuron population in both treatment groups (Fig. 6). Cardiac-projecting SG neurons had an overall higher percentage of coupled neurons (5.1 ± 2.7%) when compared with BAT-projecting SG neurons [2.4 ± 1.7%; Fig. 6, *inset*; three-way ANOVA, comparing cell type (Cardiac/BAT), treatment (MI/sham), and side (left/right), Holm–Sidak post hoc comparisons, $P = 0.002$]. Treatment and side did not have an effect on the percentage of coupled cells in the SG (Fig. 6).

Dendritic Trees of Cardiac-Projecting Neurons Are Smaller in Left SG and Larger in Right SG after MI

To test our hypothesis that morphological changes to cardiac-projecting SG neuron dendritic arbors would be present

Table 1. *Number of labeled cardiac- and BAT-projecting neurons present and 3-D-reconstructed in SGs*

	Sham		Myocardial Infarction	
Cell Type/Neurons	Left	Right	Left	Right
Cardiac				
Labeled	154.0 ± 22.4	146.8 ± 49.7	123.0 ± 24.3	127.8 ± 63.7
Soma reconstructed	31	22	32	45
BAT				
Labeled	219.3 ± 119.3	216.3 ± 116.6	197.2 ± 91.3	86.0 ± 45.1
Soma reconstructed	20	13	35	29

Number of labeled projection neurons per stellate ganglion (SG) counted in ×20 low-magnification confocal scans are expressed as means ± SD; $n = 4$ sham (2 males, 2 females) and myocardial infarction mice (3 males, 2 females). "Soma reconstructed" represents total number of neuronal somas three-dimensional (3-D) rendered per treatment group. No statistical differences, separate two-way ANOVAs on cardiac and brown adipose tissue (BAT) groups.

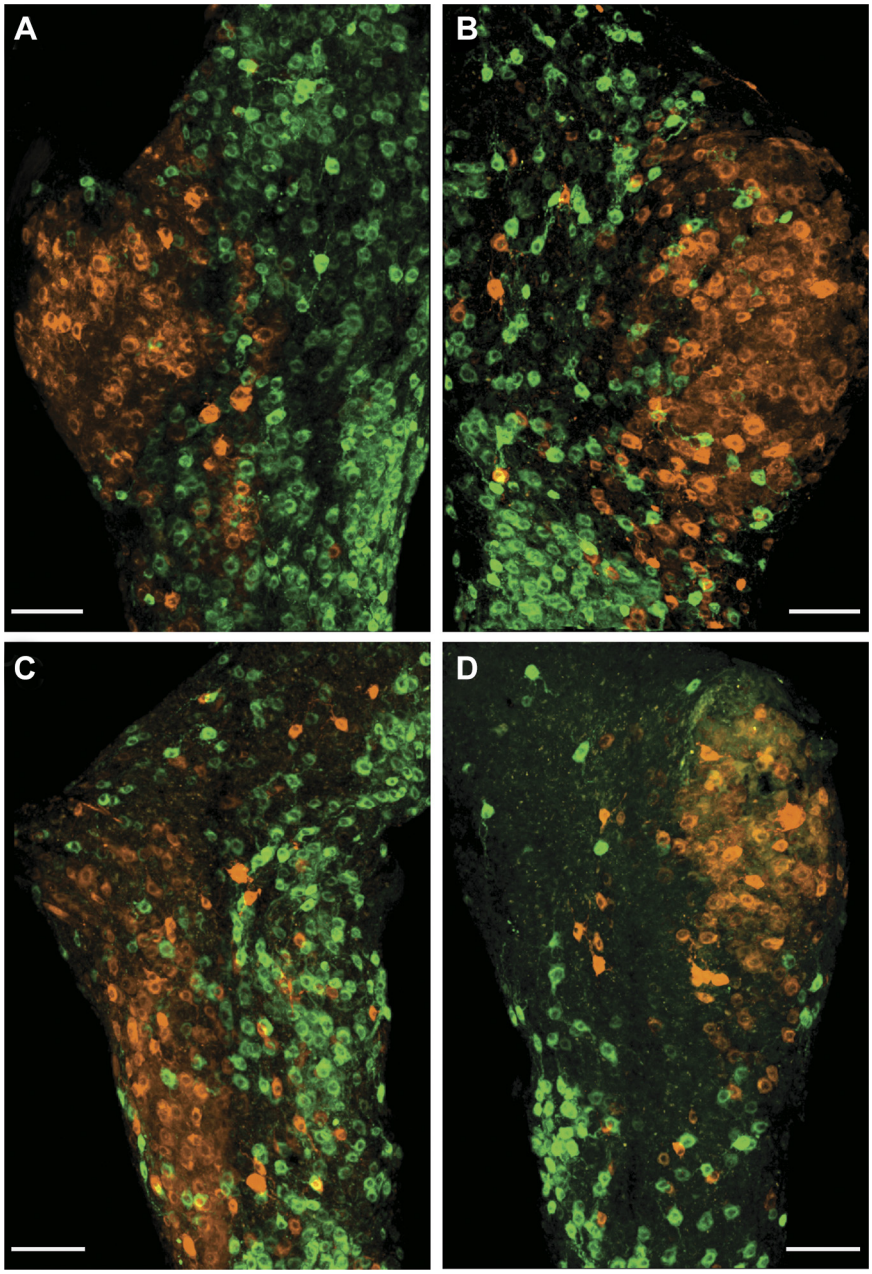

Figure. 2. Representative confocal micrographs of cardiac-projecting (orange) and brown adipose tissue (BAT)-projecting (green) stellate ganglia (SG) neurons from the left (*A* and *C*) and right (*B* and *D*) SG of sham (*A* and *B*) and myocardial infarction (MI; *C* and *D*) mice. Scale bars = 100 μm.

1 wk after MI, the dendrites of cardiac- and BAT-projecting SG neurons were reconstructed and analyzed for the number of primary dendrites, branch points, and total dendritic tree length (Table 2). There were no differences in the number of primary dendrites (two-way ANOVA) or branch points (Kruskal–Wallis one-way ANOVA on ranks) in cardiac-projecting neurons among the groups. However, dendritic tree lengths of cardiac-projecting neurons were impacted by treatment and side (Table 2 and Fig. 7; two-way ANOVA, significant interaction, $P = 0.002$). Within the sham control group, the dendritic tree lengths were significantly longer in the left SG than the right (Holm–Sidak post hoc comparisons, $P = 0.04$). This pattern was reversed within the MI group in which the dendritic tree lengths of cardiac-projecting neurons in the left SGs were shorter than the dendritic tree lengths in the right SG (Holm–Sidak post hoc comparisons, $P = 0.01$). The impact of MI was also demonstrated with significant differences in dendritic tree lengths between the MI and sham SGs on the left (Holm–Sidak post hoc comparisons, $P = 0.02$) and right ($P = 0.03$). In BAT-projecting SG neurons, there were no differences in the number of primary dendrites, branch points, or total dendritic length per neuron among the groups (Table 2; two-way ANOVAs).

VAChT Puncta Density Does Not Change in Cardiac-Projecting SG Neurons after MI

In addition to assessing SG neuron structural remodeling following MI, we determined the density of cholinergic inputs onto cardiac-projecting SG somas (Fig. 8 and Table 3). The number of VAChT-immunolabeled puncta within 0.5 mm of each soma surface was not impacted 1

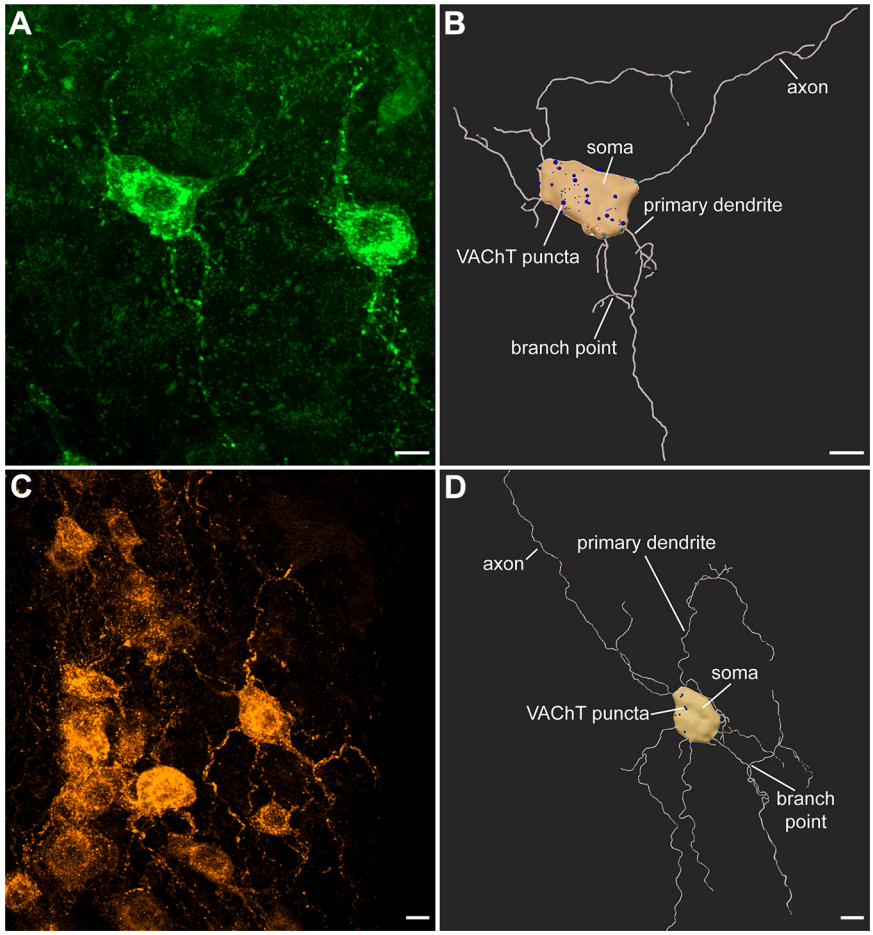

Figure 3. Representative confocal micrographs and Imaris three-dimensional (3-D) renderings of a brown adipose tissue (BAT)-projecting (*A* and *B*) and a cardiac-projecting (*C* and *D*) stellate ganglia (SG) neuron. *A*: BAT-projecting neurons in SG (green) were labeled with 0.1% CTb-488 tracer. *C*: cardiac-projecting neurons in SG (orange) were labeled with 0.1% CTb-555 tracer. Three-dimensional renderings of projection neurons were created using Imaris surfaces (somas), filaments (axons, dendrites, branch points), and spots (VAChT puncta) segmentation tools (*B* and *D*). Scale bars = 10 μm for all images. CTb, conjugated cholera toxin subunit B; VAChT, vesicular acetylcholine transporter.

wk after MI compared with the sham treatment, and there were no left/right differences (Kruskal–Wallis one-way ANOVA on ranks). Because cardiac-projecting soma size was decreased by MI in the left SG, we normalized the number of puncta per 1,000 μm^3 of soma volume and still found no difference among groups (Kruskal–Wallis one-way ANOVA on ranks).

Bone Morphogenetic Protein mRNAs Are Suppressed in Left Ventricle after MI

Bone morphogenetic proteins are required for dendritic growth in sympathetic neurons in culture (27), and they control the development, growth, and maintenance of sympathetic dendrites in vivo (28). Thus, loss of BMP signaling

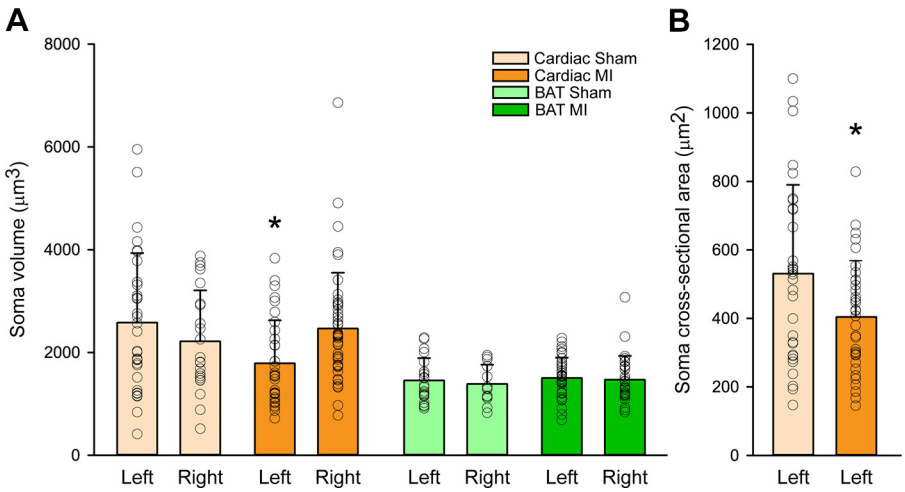

Figure 4. Myocardial infarction (MI) had a unilateral impact on soma sizes in mouse stellate ganglia (SG). *A*: soma volumes of cardiac neurons in left SGs were significantly smaller 1 wk after MI as compared with somas in the left SG of sham controls. There were no changes in right SG after MI or in brown adipose tissue (BAT) soma sizes across groups. *B*: soma cross-sectional areas for cardiac-projecting neurons in left SGs from MI-treated animals were also significantly smaller than sham controls. Bars represent means ± SD, and open circles represent individual soma volumes in each SG; $n = 4$ sham, 5 MI mice. Left cardiac MI vs. left cardiac sham; Kruskal–Wallis one-way ANOVA on ranks with Dunn's post hoc pairwise comparisons (*A*) and unpaired Welch's *t* test (*B*). $*P < 0.05$.

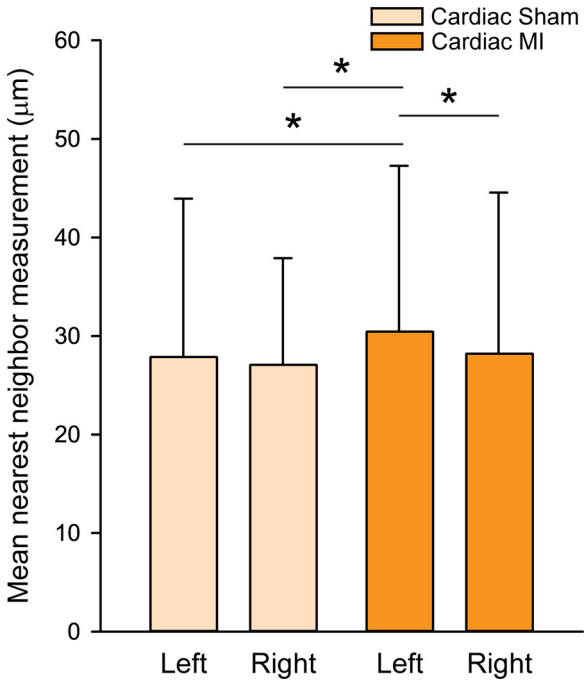

Figure 5. Myocardial infarction (MI) increased the distances measured between cardiac-projecting neurons in the left stellate ganglia (SG) compared with sham left and right and MI right. Bars represent means nearest neighbor distance measurement ± SD; $n = 4$ sham, 5 MI mice; cardiac left and right sham vs. cardiac left and right MI comparisons, Kruskal–Wallis one-way ANOVA on ranks with Dunn's post hoc pairwise comparisons: $^*P < 0.05$.

might underlie the decreased dendritic tree size observed in left SG 1 wk after MI. Neurons access BMPs both from glia within ganglia (29) and via retrograde transport from target tissues (30). As a first step to determine if the loss of retrograde BMP signaling from the damaged left ventricle (LV) might contribute to decreased dendritic tree size in cardiac neurons within the left SG, we used real-time PCR to quantify multiple BMP mRNAs known to be expressed in the heart. We compared LV from unoperated control hearts to LV taken 24 h after ischemia-reperfusion. All BMP genes that we assayed were suppressed significantly 24 h after MI (Fig. 9). This suggests a subsequent loss of BMP protein in the days after MI that could contribute to decreased dendrite length in the left SG a week after injury.

Spontaneous Neuronal Activity Increased in Left Cardiac-Projecting SG Neurons after MI

Whole cell patch-clamp recordings of cardiac-projecting left SG neurons were used to determine if MI leads to changes in neural activity (Fig. 10). Following MI, the frequency of spontaneous excitatory postsynaptic currents (sEPSCs) was significantly increased in cardiac-projecting neurons from the left SG after MI (2.67 ± 1.7 events/s, mean ± SD, $n = 6$ cells from 4 mice) compared with sham (0.63 ± 0.52 events/s, mean ± SD, $n = 10$ cells from 7 mice, $P = 0.03$, two-tailed unpaired Welch's t test). Amplitudes of sEPSCs trended higher after MI (38.0 ± 6.6 pA, mean ± SD, $n = 6$ cells from 4 mice) but were not significantly different than sham (30.4 ± 20.4 pA, mean ± SD, $n = 10$ cells from 5 mice, $P = 0.07$, two-tailed unpaired Welch's t test). These data suggest that cardiac neural activity is increased within left stellate ganglia following MI.

DISCUSSION

Cardiac ischemia-reperfusion induced structural remodeling of sympathetic neurons that project to the heart from the SG at 1 wk following the injury. The current study revealed that morphological plasticity observed in neuronal cell body size and dendrite length was specific to the cardiac-projecting SG neuron population, as MI did not influence BAT-projecting SG neurons residing in the same ganglia. Using both volume and area analyses, we found a significant reduction in cell body size of cardiac-projecting neurons in the left SG 1

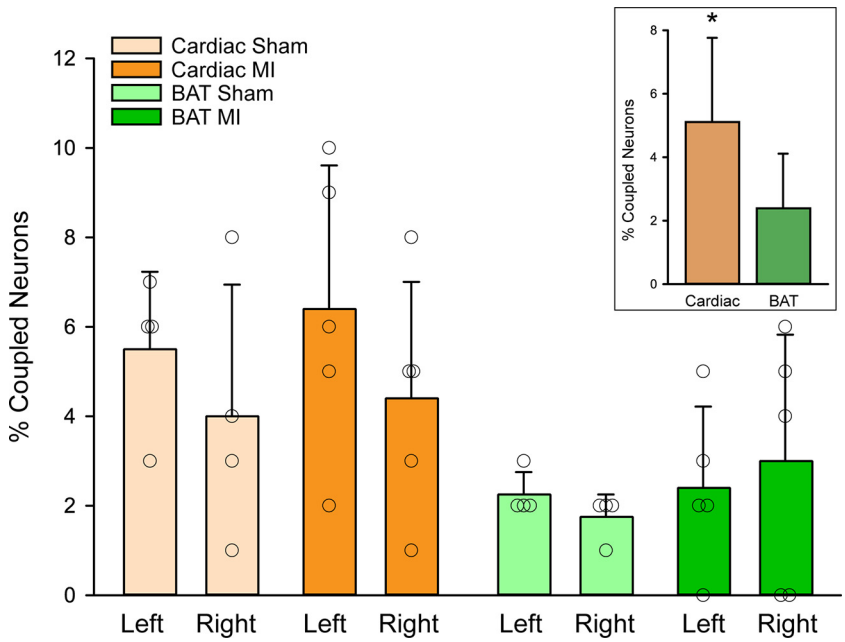

Figure 6. Cardiac-projecting stellate ganglia (SG) neurons have an overall higher percentage of neurons in direct contact ("coupled") compared with brown adipose tissue (BAT)-projecting SG neurons (*inset*). There was no difference found between treatment groups or left/right SGs. Percentage of coupled projection neurons was calculated from the total number of projection neurons in each ×20 low-magnification confocal scan. Myocardial infarction (MI) did not impact the number of projection neurons in contact with like projection neurons in either population. Bars represent means ± SD, individual dots are means percentage per SG examined; $n = 4$ sham, 5 MI mice. Cardiac vs. BAT, three-way ANOVA, comparing cell type (cardiac/BAT), treatment (MI/sham), and side (left/right), Holm–Sidak post hoc comparisons: $^*P = 0.002$.

Table 2. *Projection neuron dendritic arborization analysis*

	Sham		Myocardial Infarction	
	Left	Right	Left	Right
Neurons analyzed, *n*				
Cardiac	16	12	17	20
BAT	11	6	18	11
Primary dendrites, μm				
Cardiac	5.4 ± 2.4	4.3 ± 2.0	4.6 ± 1.4	4.9 ± 1.8
BAT	4.5 ± 2.0	6.3 ± 2.4	5.2 ± 2.4	5.7 ± 1.2
Branch points, μm				
Cardiac	9.3 ± 7.0	6.2 ± 3.7	8.9 ± 9.8	7.9 ± 5.8
BAT	4.6 ± 3.7	4.5 ± 3.0	5.9 ± 5.0	5.4 ± 5.3
Dendritic tree length, μm				
Cardiac	543.9 ± 247.6#	358.3 ± 177.9	349.2 ± 180.8*#	549.4 ± 276.6*
BAT	276.9 ± 157.8	234.2 ± 113.5	279.0 ± 137.9	307.1 ± 148.7

Values for neurons analyzed (*n*) are total numbers of projection neurons analyzed using Imaris. Numbers of primary dendrites and branch points and dendritic tree lengths (μm) are expressed as means ± SD. See Fig. 7 for a graphical representation of cardiac-projecting neuron dendritic tree lengths. Two-way ANOVA with Holm–Sidak post hoc comparisons when appropriate (cardiac and brown adipose tissue (BAT) primary dendrites, BAT branch points, cardiac and BAT dendritic tree length); Kruskal–Wallis one-way ANOVA on ranks (cardiac branch points). Myocardial infarction vs. sham, $*P < 0.05$ vs. corresponding SG on the same side; left vs. right, $\#P < 0.05$ between sides within a treatment group.

wk following MI, as well as a reduced dendritic tree length in the left SG neurons. These changes were specific to cardiac neurons in the left stellate, which are the primarily source of innervation to the damaged left ventricle. This structural plasticity coincided with an increase in the frequency of spontaneous EPSCs in left cardiac-projecting SG neurons 1 wk following MI, disproving our hypothesis that increased dendritic tree size contributed to enhanced sympathetic activity after MI.

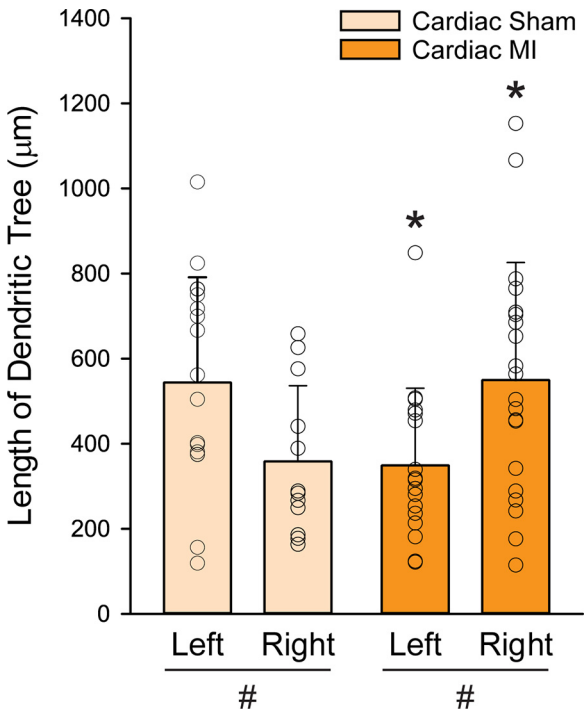

Figure 7. Sham stellate ganglia (SG) demonstrate a difference in the length of the dendritic tree between left and right sides and myocardial infarction (MI) impacts the dendritic arborization on both sides compared with sham. Bars represent the means ± SD, and the open circles represent individual values for each projection neuron in that group; $n = 4$ sham, 5 MI mice. Two-way ANOVA with Holm–Sidak post hoc comparisons, sham vs. MI, $*P < 0.05$ vs. corresponding sham SG on the same side; left vs. right, $\#P < 0.05$ between sides within a treatment group.

Target-Specific Regulation of Cell Morphology and Asymmetry

Our target-specific retrograde tract-tracing approach to assessing the impact of MI on sympathetic neuron populations allowed for the identification of subsets of neurons based on their innervated targets, an advancement from previous studies. We previously found that cardiac-projecting neurons were larger on average than BAT-projecting neurons (20), and sham animals in the current study confirmed that finding. This is consistent with early studies of sympathetic ganglia that identified differences in neuronal size and dendrite morphology based on the target innervated (31). We hypothesized that MI would cause structural remodeling in cardiac-projecting SG neurons, but not BAT-projecting SG neurons, and we found that was the case. However, we found that MI induced asymmetric changes in cardiac neuron soma size and dendritic tree length, which may be partially attributed to the location of the infarct. We observed soma size and dendritic shrinkage in left cardiac-projecting SG neurons compared with static soma size and dendritic lengthening in right cardiac-projecting SGs. It is notable that in sham animals, there was no difference in cardiac SG soma size, but there was asymmetry in the dendritic tree size in cardiac-projecting neurons. Asymmetry in cardiac sympathetic innervation has been documented in a variety of species (32), and this may contribute to differences in dendritic tree arborization between left and right cardiac SG neurons.

Changes in SG Neuronal Size Vary across Studies

Our study used an ischemia-reperfusion model in mice to produce an MI. The inflammatory response, scar formation, and time course of nerve regeneration after ischemia-reperfusion is distinct from that induced by chronic ischemia (24, 33–35). Both models are clinically relevant and understanding the impact of each type of cardiac injury on sympathetic nerves is important. Using retrograde label to identify specific neuronal populations, we found a significant reduction

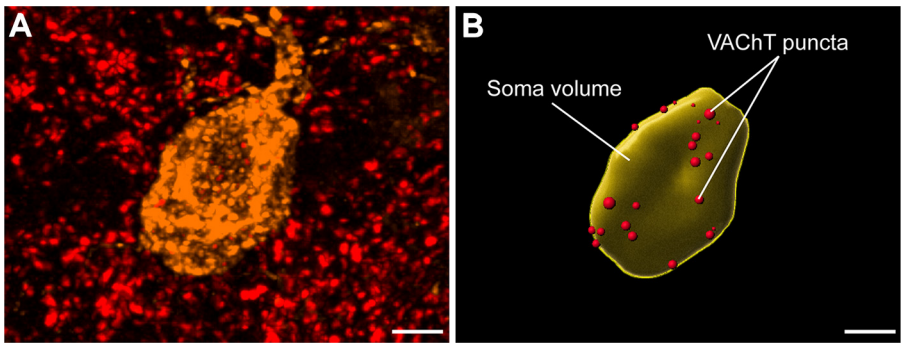

Figure 8. Representative cardiac-projecting neuron in the stellate ganglia (SG) apposed by vesicular acetylcholine transporter (VAChT)-labeled puncta. *A*: confocal micrograph of a cardiac-projecting neuron in SG (orange) labeled with 0.1% CTb-555 tracer surrounded by VAChT-labeled puncta (red). *B*: three-dimensional renderings of the soma volume (yellow surface) and the VAChT puncta (red spots) allow for measurements of neuronal size and the number of puncta apposed to the cell surface. Scale bars = 5 μm.

in cell body size for cardiac-projecting neurons in the left SG 1 wk after MI. That contrasts with previous studies reporting increases in neuronal size after chronic ischemia MI or nonischemic cardiomyopathy. One such study performed an occlusion on the right coronary artery or left circumflex artery in pigs and found an increase in soma size in both the right and left SG 5 wk later, regardless of injury site (9). Similarly, a study comparing human stellates from patients undergoing sympathectomy for ventricular arrhythmias found significant increases in soma size in stellates from patients with ischemic (cardiac scar) and nonischemic cardiomyopathy compared with controls (11). Something these studies have in common is they quantified cell size much later than 1 wk after the cardiac injury, and neuronal morphology may change over time.

A more recent study examined changes in the superior cervical ganglion (SCG) at several time points after coronary artery ligation (36). Ge and colleagues did not analyze the small subset of cardiac neurons in the SCG (16), but instead compared sympathetic neurons near the carotid body with those farther away. They identified increased soma size in the SCG 1 wk after MI, but only in neurons near the carotid body and not elsewhere. This is consistent with our observation that sympathetic neurons do not all remodel in the same manner after MI. These data support the conclusion that access to differing local and target environments plays a role in driving selective neuroplasticity.

Retrograde signaling by target-derived nerve growth factor (NGF) regulates sympathetic neuron size in adult animals (37, 38), and increased transport of NGF to stellate ganglia after MI is thought to contribute to the increased cell size seen in studies carried out several weeks after injury. NGF expression increases in the heart across multiple species after both ischemia and ischemia-reperfusion, with the highest levels of NGF observed within the infarct (33, 39–41). Zhou and colleagues (40) showed that NGF protein content but not mRNA was elevated in dog left stellate up to 1 mo after MI caused by chronic ischemia, suggesting elevated retrograde transport from the heart. In addition to high NGF in the heart, they identified substantial reinnervation of the infarct and hyperinnervation of other myocardium by 7 days after MI, all of which could contribute to increased retrograde NGF transport and larger soma size seen by others at later time points. In contrast, our ischemia-reperfusion injury generates significant sympathetic axon degeneration within the left ventricle in the first several days after MI (42, 43), and regenerating axons are excluded from entering the NGF-enriched infarct for several weeks because of chondroitin sulfate proteoglycans in the scar (33, 35, 44). The loss of axons in the damaged left ventricle and exclusion from the infarct zone may result in less retrograde NGF transport to the left stellate in the first days after injury, leading to decreased cell size. The lack of shrinkage in cardiac-projecting neurons within the right stellate, which innervates primarily the right ventricle, is consistent with the idea that neurons innervating the left ventricle, which are selectively disrupted, contribute to the decreased soma size.

Table 3. *VAChT density on cardiac-projecting SG somas are unchanged 1 wk after myocardial infarction*

	Sham		Myocardial Infarction	
VAChT Puncta	Left	Right	Left	Right
Neurons analyzed, *n*	23	19	24	37
VAChT puncta				
Per neuron	49.4 ± 51.2	38.7 ± 19.0	50.0 ± 43.4	51.4 ± 39.0
Per 1,000-μm^3 soma volume	18.0 ± 9.1	20.4 ± 14.4	32.0 ± 32.3	22.6 ± 18.3

Numbers of vesicular acetylcholine transporter (VAChT) puncta per neuron and per 1,000-μm^3 soma volume are expressed as means ± SD; *n*, total numbers of projection neurons analyzed using Imaris. No significant differences, Kruskal–Wallis one-way ANOVA on ranks.

Regulation of Dendritic Tree Size

In addition to reduced cell volume, we found that left SG cardiac-projecting neurons had a smaller overall dendritic tree size after MI compared with the left SG in sham animals. Decreased retrograde NGF may contribute to dendritic shrinkage, as a basal level of NGF is required for stimulation of dendrite growth (45). However, NGF is not the major controller of dendrite size in sympathetic neurons. BMPs are the primary factors regulating the development, growth, and maintenance of sympathetic dendrites in vitro (27) and in vivo (28), through activation of the BMPR1a receptor (28). In contrast to the many studies examining NGF expression in the heart after MI, BMP expression was unknown. Therefore, we quantified BMP mRNA in the left ventricle a day after ischemia-reperfusion and found that all of the six BMP mRNAs we assayed were decreased significantly just 24 h after injury. This suggests a loss of BMP protein in the days after MI that, in combination with axon degeneration, would lead to the loss of retrograde BMP signaling. Although sympathetic neurons can also access BMPs released by glia cells

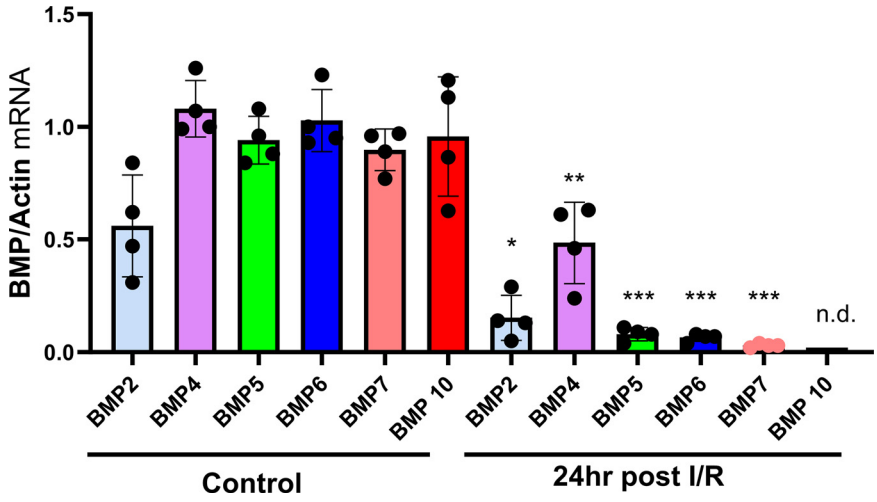

Figure 9. Bone morphogenetic protein (BMP) genes are suppressed in the left ventricle (LV) 24 h after myocardial infarction (MI). Gene expression in unoperated control and MI LVs were assayed 24 h after ischemia-reperfusion. BMP mRNA was normalized to actin mRNA in the same sample. Bars represent the means ± SD, and circles represent individual values for each mouse; $n = 4$ mice/treatment group (2 males, 2 females). Control vs. 24 H post-MI, unpaired Welch's t test: BMP2, $^{*}P = 0.03$; BMP4, $^{**}P = 0.002$; BMP5, $^{***}P = 0.0002$; BMP6, $^{***}P = 0.0007$; BMP7, $^{***}P = 0.0003$. nd, not detected.

(29), the loss of retrograde signaling would contribute to decreased dendritic tree size after MI.

Another set of factors that may contribute to a selective decrease in dendrites within cardiac-projecting left stellate neurons are inflammatory cytokines acting through the gp130 cytokine receptor, which can cause dendrite retraction in sympathetic neurons (46). Several of these cytokines are elevated in the heart after MI [reviewed by Fischer and Hilfiker-Kleiner (47)]. Activation of gp130 on cardiac sympathetic neurons contributes to axon regeneration in the first few days after MI (48) and later stimulates the induction of cholinergic neurotransmission (49). These cytokines are elevated in both sympathetic ganglia and peripheral tissues after axon injury (50), so disrupted retrograde transport from the heart would not necessarily prevent activation of gp130 in left stellate cardiac neurons. Indeed, the loss of retrograde NGF signaling can enhance the response of sympathetic neurons to glial-derived cytokines (51) and thus a combination of changes in growth factors and cytokines might contribute to selective dendrite retraction after MI.

Changes in Neuronal Dispersion in SG after MI

MI did not significantly impact the number of cardiac-projecting SG cells or their qualitative distribution, which suggests that the MI surgery begun 10 min after tracer injection did not interfere with retrograde neuronal transport of the CTb tracer. However, cell dispersion (distance between neighboring cells) was increased between left cardiac-projecting SG neurons after MI. This might be due in part to the reduction in neuron size among left SG cardiac neurons, but other factors likely contribute including increased infiltration of immune cells and changes in satellite glia (52, 53). It is unclear whether there is any physiological significance to these changes in neuronal dispersion.

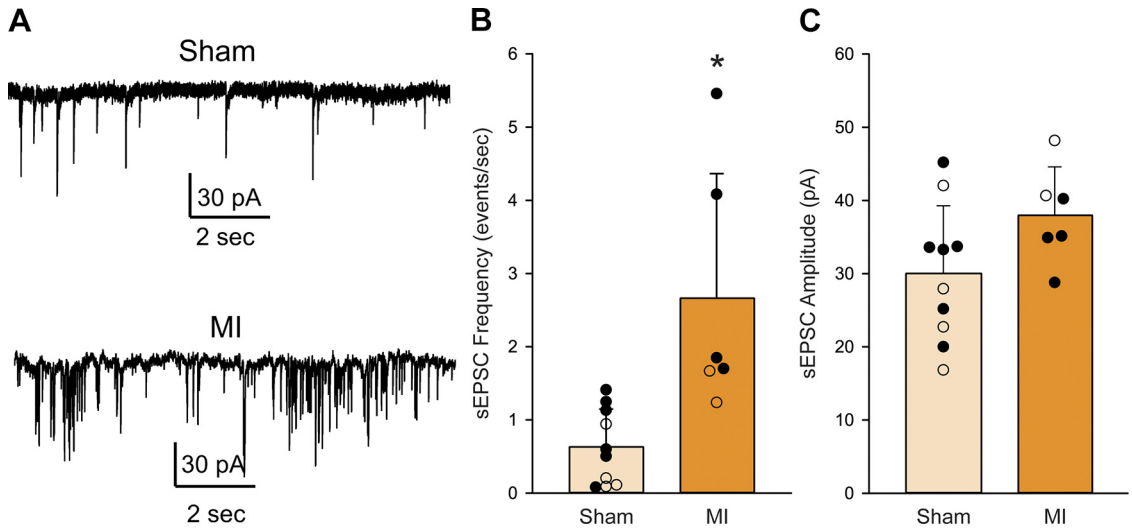

Figure 10. Neuronal activity in cardiac-projecting neurons was impacted by myocardial infarction (MI). *A*: representative recordings from sham and MI ganglia. *B*: MI caused a significant increase in the frequency of spontaneous excitatory postsynaptic currents (sEPSCs). *C*: amplitude trended higher but was not significantly different ($P = 0.07$). All cells were recorded from the left stellate ganglia (SG). Bars are means ± SD, filled circles represent cells back labeled from the heart and open circles represent cells located in the cardiac pole of unlabeled SG. MI, $n = 6$ cells from 4 mice; sham, $n = 10$ cells from 7 mice. MI vs. sham, unpaired Welch's t test. $^{*}P = 0.03$.

Cholinergic Synapses and Functional Changes in Left Cardiac-Projecting SG Neurons

The density of VAChT-immunoreactive presynaptic cholinergic inputs apposed to cardiac-projecting SG neurons was unchanged 1 wk following MI, suggesting that functional changes following MI are not driven by increased synapses on the cell soma. These findings, combined with our previous study, show a stable number of VAChT inputs per unit membrane of both cardiac- and BAT-projecting SG neurons that may be highly regulated. A previous study in rabbits showed significant increases in the density of cholinergic fibers within the SG 1 wk and 1 mo following an MI caused by chronic ischemia (19). This suggests sprouting of either preganglionic projections from the spinal cord or the newly identified cholinergic collateral projections from postganglionic sympathetic neurons (26). It is possible that there are increased cholinergic inputs to dendrites, which we were unable to measure in this study, or that activity of presynaptic inputs is altered without changes in number of presumed synaptic inputs. Our electrophysiology data revealed significantly more spontaneous EPSCs in left SG explanted after MI compared with sham. The increase in sEPSC frequency is consistent with increased neurotransmission within the ganglion by cholinergic collaterals, as is the trend toward increased sEPSC amplitude after MI. Our previous studies showed that sEPSCs within the ganglion are blocked by tetrodotoxin and hexamethonium, and thus result from action potential-evoked cholinergic transmission. (26) Additional studies will be required to elucidate the full mechanism underlying this increase in neuronal activity, which may include changes in presynaptic transmitter release, or alterations in the number, type, and distribution of ion channels along the cell membrane.

Limitations

Retrograde tract tracing affords the observer the opportunity to assess neuron morphology in whole mounted SG slides, and using Imaris 3-D image reconstruction software also has allowed us to effectively trace dendritic arbors that may otherwise be untraceable using typical histological sectioning methods. One limitation of this approach is that the timeline for optimal neuronal labeling with CTb-conjugated tracers is confined to just 1 wk after tracer injection (20). This limitation restricts our ability to study target-specific neuron populations at various time points following MI, as the pericardium is disrupted by the LAD ligation procedure and thus cardiac-specific labeling cannot be carried out after the initial surgery.

Conclusions

We found both morphological and functional changes specifically in cardiac-projecting left SG neurons after ischemia-reperfusion injury, with no changes in BAT-projecting neurons within the same ganglia of the same animal. These findings support the idea that the mechanisms underlying this neuronal plasticity are mediated by cell-specific signaling mechanisms rather than endocrine or paracrine actions within the stellate ganglion that would globally impact all neurons. Future studies are needed to determine the specific molecules and signaling mechanisms underlying these structural and functional changes.

DATA AVAILABILITY

Data will be made available upon reasonable request.

ACKNOWLEDGMENTS

We thank members of the Aicher and Habecker laboratories for supporting the team conducting these studies, especially Diana Parrish and Kurt Gritman for providing important technical assistance. We are also grateful for the support and expertise of the staff of the OHSU Advanced Light Microscopy Core.

Graphical abstract was created with a licensed version of Biorender.com.

GRANTS

This work was supported by National Heart, Lung, and Blood Institute Grant HL146833 (to B. A. Habecker principal investigator; S. A. Aicher coinvestigator).

DISCLOSURES

No conflicts of interest, financial or otherwise, are declared by the authors.

AUTHOR CONTRIBUTIONS

S.L.I., B.A.H., and S.A.A. conceived and designed research; M.S.B., M-H.L., C.J.A., and B.A.H. performed experiments; M.S.B., T.C.B., M-H.L., D.M.H., C.M.D.M., and C.J.A. analyzed data; S.L.I., B.A.H., and S.A.A. interpreted results of experiments; M.S.B., T.C.B., M-H.L., D.M.H., C.M.D.M., and B.A.H. prepared figures; M.S.B., T.C.B., and S.A.A. drafted manuscript; M.S.B., T.C.B., M-H.L., D.M.H., C.M.D.M., C.J.A., S.L.I., B.A.H., and S.A.A. edited and revised manuscript; M.S.B., T.C.B., M-H.L., D.M.H., C.M.D.M., C.J.A., S.L.I., B.A.H., and S.A.A. approved final version of manuscript.

REFERENCES

1. **Chugh SS**, **Reinier K**, **Teodorescu C**, **Evanado A**, **Kehr E**, **Al Samara M**, **Mariani R**, **Gunson K**, **Jui J.** Epidemiology of sudden cardiac death: clinical and research implications. *Prog Cardiovasc Dis* 51: 213–228, 2008. doi:10.1016/j.pcad.2008.06.003.
2. **Solomon SD**, **Zelenkofske S**, **McMurray JJ**, **Finn PV**, **Velazquez E**, **Ertl G**, **Harsanyi A**, **Rouleau JL**, **Maggioni A**, **Kober L**, **White H**, **Van de Werf F**, **Pieper K**, **Califf RM**, **Pfeffer MA**; **Valsartan in Acute Myocardial Infarction Trial (VALIANT) Investigators.** Sudden death in patients with myocardial infarction and left ventricular dysfunction, heart failure, or both. *N Engl J Med* 352: 2581–2588, 2005 [Erratum in *N Engl J Med* 353: 744, 2005]. doi:10.1056/NEJMoa043938.
3. **Pouleur AC**, **Barkoudah E**, **Uno H**, **Skali H**, **Finn PV**, **Zelenkofske SL**, **Belenkov YN**, **Mareev V**, **Velazquez EJ**, **Rouleau JL**, **Maggioni AP**, **Kober L**, **Califf RM**, **McMurray JJ**, **Pfeffer MA**, **Solomon SD**; **VALIANT Investigators.** Pathogenesis of sudden unexpected death in a clinical trial of patients with myocardial infarction and left ventricular dysfunction, heart failure, or both. *Circulation* 122: 597–602, 2010. doi:10.1161/CIRCULATIONAHA.110.940619.
4. **Freemantle N**, **Cleland J**, **Young P**, **Mason J**, **Harrison J.** beta Blockade after myocardial infarction: systematic review and meta regression analysis. *BMJ* 318: 1730–1737, 1999. doi:10.1136/bmj.318.7200.1730.
5. **Vaseghi M**, **Gima J**, **Kanaan C**, **Ajijola OA**, **Marmureanu A**, **Mahajan A**, **Shivkumar K.** Cardiac sympathetic denervation in patients with refractory ventricular arrhythmias or electrical storm: intermediate and long-term follow-up. *Heart Rhythm* 11: 360–366, 2014. doi:10.1016/j.hrthm.2013.11.028.

6. **Nademanee K**, **Taylor R**, **Bailey WE**, **Rieders DE**, **Kosar EM.** Treating electrical storm: sympathetic blockade versus advanced cardiac life support-guided therapy. *Circulation* 102: 742–747, 2000. doi:10.1161/01.cir.102.7.742.
7. **Basu S**, **Senior R**, **Raval U**, **van der Does R**, **Bruckner T**, **Lahiri A.** Beneficial effects of intravenous and oral carvedilol treatment in acute myocardial infarction. A placebo-controlled, randomized trial. *Circulation* 96: 183–191, 1997. doi:10.1161/01.cir.96.1.183.
8. **Irie T**, **Yamakawa K**, **Hamon D**, **Nakamura K**, **Shivkumar K**, **Vaseghi M.** Cardiac sympathetic innervation via middle cervical and stellate ganglia and antiarrhythmic mechanism of bilateral stellectomy. *Am J Physiol Heart Circ Physiol* 312: H392–H405, 2017. doi:10.1152/ajpheart.00644.2016.
9. **Ajijola OA**, **Yagishita D**, **Reddy NK**, **Yamakawa K**, **Vaseghi M**, **Downs AM**, **Hoover DB**, **Ardell JL**, **Shivkumar K.** Remodeling of stellate ganglion neurons after spatially targeted myocardial infarction: neuropeptide and morphologic changes. *Heart Rhythm* 12: 1027–1035, 2015. doi:10.1016/j.hrthm.2015.01.045.
10. **Han S**, **Kobayashi K**, **Joung B**, **Piccirillo G**, **Maruyama M**, **Vinters HV**, **March K**, **Lin SF**, **Shen C**, **Fishbein MC**, **Chen P-S**, **Chen LS.** Electroanatomic remodeling of the left stellate ganglion after myocardial infarction. *J Am Coll Cardiol* 59: 954–961, 2012. doi:10.1016/j.jacc.2011.11.030.
11. **Ajijola OA**, **Wisco JJ**, **Lambert HW**, **Mahajan A**, **Stark E**, **Fishbein MC**, **Shivkumar K.** Extracardiac neural remodeling in humans with cardiomyopathy. *Circ Arrhythm Electrophysiol* 5: 1010–1116, 2012. doi:10.1161/CIRCEP.112.972836.
12. **Clyburn C**, **Sepe JJ**, **Habecker BA.** What gets on the nerves of cardiac patients? Pathophysiological changes in cardiac innervation. *J Physiol* 600: 451–461, 2022. doi:10.1113/JP281118.
13. **Herring N**, **Kalla M**, **Paterson DJ.** The autonomic nervous system and cardiac arrhythmias: current concepts and emerging therapies. *Nat Rev Cardiol* 16: 707–726, 2019 [Erratum in *Nat Rev Cardiol* 16: 760, 2019]. doi:10.1038/s41569-019-0221-2.
14. **Kimura K**, **Ieda M**, **Fukuda K.** Development, maturation, and transdifferentiation of cardiac sympathetic nerves. *Circ Res* 110: 325–336, 2012. doi:10.1161/CIRCRESAHA.111.257253.
15. **Hasan W.** Autonomic cardiac innervation: development and adult plasticity. *Organogenesis* 9: 176–193, 2013. doi:10.4161/org.24892.
16. **Pardini BJ**, **Lund DD**, **Schmid PG.** Organization of the sympathetic postganglionic innervation of the rat heart. *J Auton Nerv Syst* 28: 193–201, 1989. doi:10.1016/0165-1838(89)90146-x.
17. **Francois M**, **Torres H**, **Huesing C**, **Zhang R**, **Saurage C**, **Lee N**, **Qualls-Creekmore E**, **Yu S**, **Morrison CD**, **Burk D**, **Berthoud HR**, **Munzberg H.** Sympathetic innervation of the interscapular brown adipose tissue in mouse. *Ann N Y Acad Sci* 1454: 3–13, 2019. doi:10.1111/nyas.14119.
18. **Sridharan A**, **Bradfield JS**, **Shivkumar K**, **Ajijola OA.** Autonomic nervous system and arrhythmias in structural heart disease. *Auton Neurosci* 243: 103037, 2022. doi:10.1016/j.autneu.2022.103037.
19. **Nguyen BL**, **Li H**, **Fishbein MC**, **Lin SF**, **Gaudio C**, **Chen P-S**, **Chen LS.** Acute myocardial infarction induces bilateral stellate ganglia neural remodeling in rabbits. *Cardiovasc Pathol* 21: 143–148, 2012. doi:10.1016/j.carpath.2011.08.001.
20. **Barrett MS**, **Hegarty DM**, **Habecker BA**, **Sa A.** Distinct morphology of cardiac- and brown adipose tissue-projecting neurons in the stellate ganglia of mice. *Physiol Rep* 10: e15334, 2022. doi:10.14814/phy2.15334.
21. **Kilkenny C**, **Browne W**, **Cuthill IC**, **Emerson M**, **Altman DG**, **Ncrrgw G**; **NC3Rs Reporting Guidelines Working Group.** Animal research: reporting in vivo experiments: the ARRIVE guidelines. *Br J Pharmacol* 160: 1577–1579, 2010. doi:10.1111/j.1476-5381.2010.00872.x.
22. **Parrish DC**, **Francis Stuart SD**, **Olivas A**, **Wang L**, **Nykjaer A**, **Ripplinger CM**, **Habecker BA.** Transient denervation of viable myocardium after myocardial infarction does not alter arrhythmia susceptibility. *Am J Physiol Heart Circ Physiol* 314: H415–H423, 2018. doi:10.1152/ajpheart.00300.2017.
23. **Gritman K**, **Van Winkle DM**, **Lorentz CU**, **Pennica D**, **Habecker BA.** The lack of cardiotrophin-1 alters expression of interleukin-6 and leukemia inhibitory factor mRNA but does not impair cardiac injury response. *Cytokine* 36: 9–16, 2006. doi:10.1016/j.cyto.2006.10.004.
24. **Lindsey ML**, **Brunt KR**, **Kirk JA**, **Kleinbongard P**, **Calvert JW**, **de Castro Bras LE**, **DeLeon-Pennell KY**, **Del Re DP**, **Frangogiannis NG**, **Frantz S**, **Gumina RJ**, **Halade GV**, **Jones SP**, **Ritchie RH**, **Spinale FG**, **Thorp EB**, **Ripplinger CM**, **Kassiri Z.** Guidelines for in vivo mouse models of myocardial infarction. *Am J Physiol Heart Circ Physiol* 321: H1056–H1073, 2021. doi:10.1152/ajpheart.00459.2021.
25. **Parrish DC**, **Alston EN**, **Rohrer H**, **Nkadi P**, **Woodward WR**, **Schutz G**, **Habecker BA.** Infarction-induced cytokines cause local depletion of tyrosine hydroxylase in cardiac sympathetic nerves. *Exp Physiol* 95: 304–314, 2010. doi:10.1113/expphysiol.2009.049965.
26. **Clyburn C**, **Li MH**, **Ingram SL**, **Andresen MC**, **Habecker BA.** Cholinergic collaterals arising from noradrenergic sympathetic neurons in mice. *J Physiol* 601: 1247–1264, 2023. doi:10.1113/JP284059.
27. **Lein P**, **Johnson M**, **Guo X**, **Rueger D**, **Higgins D.** Osteogenic protein-1 induces dendritic growth in rat sympathetic neurons. *Neuron* 15: 597–605, 1995. doi:10.1016/0896-6273(95)90148-5.
28. **Majdazari A**, **Stubbusch J**, **Muller CM**, **Hennchen M**, **Weber M**, **Deng C-X**, **Mishina Y**, **Schutz G**, **Deller T**, **Rohrer H.** Dendrite complexity of sympathetic neurons is controlled during postnatal development by BMP signaling. *J Neurosci* 33: 15132–15144, 2013. doi:10.1523/JNEUROSCI.4748-12.2013.
29. **Lein PJ**, **Beck HN**, **Chandrasekaran V**, **Gallagher PJ**, **Chen H-L**, **Lin Y**, **Guo X**, **Kaplan PL**, **Tiedge H**, **Higgins D.** Glia induce dendritic growth in cultured sympathetic neurons by modulating the balance between bone morphogenetic proteins (BMPs) and BMP antagonists. *J Neurosci* 22: 10377–10387, 2002. doi:10.1523/JNEUROSCI.22-23-10377.2002.
30. **Hodge LK**, **Klassen MP**, **Han BX**, **Yiu G**, **Hurrell J**, **Howell A**, **Rousseau G**, **Lemaigre F**, **Tessier-Lavigne M**, **Wang F.** Retrograde BMP signaling regulates trigeminal sensory neuron identities and the formation of precise face maps. *Neuron* 55: 572–586, 2007. doi:10.1016/j.neuron.2007.07.010.
31. **Andrews TJ**, **Thrasivoulou C**, **Nesbit W**, **Cowen T.** Target-specific differences in the dendritic morphology and neuropeptide content of neurons in the rat SCG during development and aging. *J Comp Neurol* 368: 33–44, 1996. doi:10.1002/(SICI)1096-9861(19960422)368:1<33::AID-CNE3>3.0.CO;2-L.
32. **Zandstra TE**, **Notenboom RGE**, **Wink J**, **Kies P**, **Vliegen HW**, **Egorova AD**, **Schalij MJ**, **De Ruiter MC**, **Jongbloed MRM.** Asymmetry and heterogeneity: part and parcel in cardiac autonomic innervation and function. *Front Physiol* 12: 665298, 2021. doi:10.3389/fphys.2021.665298.
33. **Gardner RT**, **Habecker BA.** Infarct-derived chondroitin sulfate proteoglycans prevent sympathetic reinnervation after cardiac ischemia-reperfusion injury. *J Neurosci* 33: 7175–7183, 2013. doi:10.1523/JNEUROSCI.5866-12.2013.
34. **Lindsey ML**, **de Castro Bras LE**, **DeLeon-Pennell KY**, **Frangogiannis NG**, **Halade GV**, **O'Meara CC**, **Spinale FG**, **Kassiri Z**, **Kirk JA**, **Kleinbongard P**, **Ripplinger CM**, **Brunt KR.** Reperfused vs. nonreperfused myocardial infarction: when to use which model. *Am J Physiol Heart Circ Physiol* 321: H208–H213, 2021. doi:10.1152/ajpheart.00234.2021.
35. **Blake MR**, **Parrish DC**, **Staffenson MA**, **Johnson MA**, **Woodward WR**, **Habecker BA.** Loss of chondroitin sulfate proteoglycan sulfation allows delayed sympathetic reinnervation after cardiac ischemia-reperfusion. *Physiol Rep* 11: e15702, 2023. doi:10.14814/phy2.15702.
36. **Ge Y**, **van Roon L**, **van Gils JM**, **Geestman T**, **van Munsteren CJ**, **Smits AM**, **Goumans M**, **DeRuiter MC**, **Jongbloed MRM.** Acute myocardial infarction induces remodeling of the murine superior cervical ganglia and the carotid body. *Front Cardiovasc Med* 9: 758265, 2022. doi:10.3389/fcvm.2022.758265.
37. **Davis BM**, **Wang HS**, **Albers KM**, **Carlson SL**, **Goodness TP**, **McKinnon D.** Effects of NGF overexpression on anatomical and physiological properties of sympathetic postganglionic neurons. *Brain Res* 724: 47–54, 1996. doi:10.1016/0006-8993(96)00265-x.
38. **Andrews TJ.** Autonomic nervous system as a model of neuronal aging: the role of target tissues and neurotrophic factors. *Microsc Res Tech* 35: 2–19, 1996. doi:10.1002/(SICI)1097-0029(19960901)35:1<2::AID-JEMT2>3.0.CO;2-V.
39. **Meloni M**, **Caporali A**, **Graiani G**, **Lagrasta C**, **Katare R**, **Van Linthout S**, **Spillmann F**, **Campesi I**, **Madeddu P**, **Quaini F**, **Emanueli C.** Nerve growth factor promotes cardiac repair following myocardial infarction. *Circ Res* 106: 1275–1284, 2010. doi:10.1161/CIRCRESAHA.109.210088.

40. **Zhou S**, **Chen LS**, **Miyauchi Y**, **Miyauchi M**, **Kar S**, **Kangavari S**, **Fishbein MC**, **Sharifi B**, **Chen PS.** Mechanisms of cardiac nerve sprouting after myocardial infarction in dogs. *Circ Res* 95: 76–83, 2004. doi:10.1161/01.RES.0000133678.22968.e3.
41. **Hiltunen JO**, **Laurikainen A**, **Vakeva A**, **Meri S**, **Saarma M.** Nerve growth factor and brain-derived neurotrophic factor mRNAs are regulated in distinct cell populations of rat heart after ischaemia and reperfusion. *J Pathol* 194: 247–253, 2001. doi:10.1002/path.878.
42. **Li W**, **Knowlton D**, **Van Winkle DM**, **Habecker BA.** Infarction alters both the distribution and noradrenergic properties of cardiac sympathetic neurons. *Am J Physiol Heart Circ Physiol* 286: H2229–H2236, 2004. doi:10.1152/ajpheart.00768.2003.
43. **Lorentz CU**, **Parrish DC**, **Alston EN**, **Pellegrino MJ**, **Woodward WR**, **Hempstead BL**, **Habecker BA.** Sympathetic denervation of periinfarct myocardium requires the p75 neurotrophin receptor. *Exp Neurol* 249: 111–119, 2013. doi:10.1016/j.expneurol.2013.08.015.
44. **Gardner RT**, **Wang L**, **Lang BT**, **Cregg JM**, **Dunbar CL**, **Woodward WR**, **Silver J**, **Ripplinger CM**, **Habecker BA.** Targeting protein tyrosine phosphatase sigma after myocardial infarction restores cardiac sympathetic innervation and prevents arrhythmias. *Nat Commun* 6: 6235, 2015. doi:10.1038/ncomms7235.
45. **Courter LA**, **Shaffo FC**, **Ghogha A**, **Parrish DJ**, **Lorentz CU**, **Habecker BA**, **Lein PJ.** BMP7-induced dendritic growth in sympathetic neurons requires p75(NTR) signaling. *Dev Neurobiol* 76: 1003–1013, 2016. doi:10.1002/dneu.22371.
46. **Guo X**, **Chandrasekaran V**, **Lein P**, **Kaplan PL**, **Higgins D.** Leukemia inhibitory factor and ciliary neurotrophic factor cause dendritic retraction in cultured rat sympathetic neurons. *J Neurosci* 19: 2113–2121, 1999. doi:10.1523/JNEUROSCI.19-06-02113.1999.
47. **Fischer P**, **Hilfiker-Kleiner D.** Survival pathways in hypertrophy and heart failure: the gp130-STAT axis. *Basic Res Cardiol* 102: 393–411, 2007. doi:10.1007/s00395-007-0674-z.
48. **Pellegrino MJ**, **Habecker BA.** STAT3 integrates cytokine and neurotrophin signals to promote sympathetic axon regeneration. *Mol Cell Neurosci* 56: 272–282, 2013. doi:10.1016/j.mcn.2013.06.005.
49. **Olivas A**, **Gardner RT**, **Wang L**, **Ripplinger CM**, **Woodward WR**, **Habecker BA.** Myocardial infarction causes transient cholinergic transdifferentiation of cardiac sympathetic nerves via gp130. *J Neurosci* 36: 479–488, 2016 [Erratum in *J Neurosci* 40: 8205, 2020]. doi:10.1523/JNEUROSCI.3556-15.2016.
50. **Zigmond RE**, **Sun Y.** Regulation of neuropeptide expression in sympathetic neurons. Paracrine and retrograde influences. *Ann N Y Acad Sci* 814: 181–197, 1997. doi:10.1111/j.1749-6632.1997.tb46157.x.
51. **Shadiack AM**, **Vaccariello SA**, **Sun Y**, **Zigmond RE.** Nerve growth factor inhibits sympathetic neurons' response to an injury cytokine. *Proc Natl Acad Sci USA* 95: 7727–7730, 1998. doi:10.1073/pnas.95.13.7727.
52. **Ajijola OA**, **Hoover DB**, **Simerly TM**, **Brown TC**, **Yanagawa J**, **Biniwale RM**, **Lee JM**, **Sadeghi A**, **Khanlou N**, **Ardell JL**, **Shivkumar K.** Inflammation, oxidative stress, and glial cell activation characterize stellate ganglia from humans with electrical storm. *JCI Insight* 2: e94715, 2017. doi:10.1172/jci.insight.94715.
53. **Tu G**, **Li G**, **Peng H**, **Hu J**, **Liu J**, **Kong F**, **Liu S**, **Gao Y**, **Xu C**, **Xu X**, **Qiu S**, **Fan B**, **Zhu Q**, **Yu S**, **Zheng C**, **Wu B**, **Peng L**, **Song M**, **Wu Q**, **Liang S.** P2X(7) inhibition in stellate ganglia prevents the increased sympathoexcitatory reflex via sensory-sympathetic coupling induced by myocardial ischemic injury. *Brain Res Bull* 96: 71–85, 2013. doi:10.1016/j.brainresbull.2013.05.004.